ADVANCED MATERIALS TECHNOLOGIES
www.advmattechnol.de

4D Printing of Stretchable Supercapacitors via Hybrid Composite Materials

*Yihao Zhou, Charles B. Parker, Pooran Joshi, Amit K. Naskar, Jeffrey T. Glass, and Changyong Cao**

Stretchable supercapacitors (SCs) have attracted significant attention in developing power-independent stretchable electronic systems due to their intrinsic energy storage function and unique mechanical properties. Most current SCs are generally limited by their low stretchability, complicated fabrication process, and insufficient performance and robustness. This study presents a facile method to fabricate arbitrary-shaped stretchable electrodes via 4D printing of conductive composite from reduced graphene oxide, carbon nanotube, and poly(3,4-ethylenedioxythiophene) polystyrene sulfonate. The electrode patterns of an arbitrary shape can be deposited onto prestretched substrates by aerosol-jet printing, then self-organized origami (ridge) patterns are generated after releasing the substrates from holding stretchers due to the mismatched strains. The stretchable electrodes demonstrate superior mechanical robustness and stretchability without sacrificing its outstanding electrochemical performance. The symmetric SC prototype possesses a gravimetric capacitance of ≈21.7 F g^{-1} at a current density of 0.5 A g^{-1} and a capacitance retention of ≈85.8% from 0.5 to 5 A g^{-1}. A SC array with arbitrary-shaped electrodes is also fabricated and connected in series to power light-emitting diode patterns for large-scale applications. The proposed method paves avenues for scalable manufacturing of future energy-storage devices with controlled extensibility and high electrochemical performance.

1. Introduction

Advances in stretchable[1–3] and wearable electronics[4] have created increasing demand for more compatible and higher performance energy storage devices, which can be integrated and deformed together with unconventional electronics in achieving fully power-independent and stretchable systems for practical applications.[2,4,5] Recently, highly stretchable lithium-ion batteries capable of over 300% deformation have been developed with novel strategies such as self-similar serpentine interconnects[6] and origami of thin sheets.[7] In comparison with batteries, supercapacitors (SCs) have advantages of fast charge/discharge rate and long operating life, representing a promising candidate for energy-storage devices used in unconventional electronics. Existing stretchable SCs that use films or meshes of carbon nanotube (CNT) or graphene as electrodes[8] typically reach a stretchability of up to 30% to 300%. With ultra-stretchable gel electrolyte used, some SCs with CNT electrodes reported a stretchability of up to 1000%.[9] However, the fabrication of such stretchable SCs usually relies on the transfer of active material layers onto target substrates, which is a complicated, troublesome, time-consuming, and expensive process. Therefore, there is an urgent need to explore new strategies and seamless integration of the latest advances in materials and manufacturing to make stretchable and high-performance SCs.

Printing techniques offer a promising solution to the scalable manufacturing of stretchable SCs. Over the past decade, printed electronics have attracted increasing attention for the fabrication of novel electronics, such as thin-film transistors (TFTs), sensors, and energy storage devices,[1–4] owing to the unique advantages of low-cost, high-throughput, and ability for mass production. In particular, inkjet printing has many advantages, such as low-cost, direct writing, additive patterning, and scalable production, when applied to the

Dr. Y. Zhou, Prof. C. Cao
Laboratory for Soft Machines and Electronics
School of Packaging
Michigan State University
East Lansing, MI 48824, USA
E-mail: ccao@msu.edu
Dr. Y. Zhou, Dr. C. B. Parker, Prof. J. T. Glass
Department of Electrical and Computer Engineering
Duke University
Durham, NC 27708, USA
The ORCID identification number(s) for the author(s) of this article can be found under https://doi.org/10.1002/admt.202001055.

DOI: 10.1002/admt.202001055

Dr. P. Joshi
Electrical and Electronics Systems Research Division
Oak Ridge National Laboratory
Oak Ridge, TN 37831, USA
Dr. A. K. Naskar
Chemical Sciences Division
Oak Ridge National Laboratory
Oak Ridge, TN 37831, USA
Prof. C. Cao
Department of Mechanical Engineering
Department of Electrical and Computer Engineering
Michigan State University
East Lansing, MI 48824, USA

fabrication of printable electrodes. For example, graphene has been inkjet-printed to make SC electrodes,[10,11] chemical sensors,[12] and TFTs.[13] With high surface area, good electric conductivity, and low cost, graphene is one of the most promising materials for SC applications. However, it is challenging to inkjet print graphene due to its poor dispersion and aggregation in the ink.[14] Le et al. developed a method using graphene oxide (GO) as the ink to print high-quality thin films followed by a reduction process to regain the electrical properties of graphene.[10] The resultant graphene thin film electrodes showed a high specific capacitance of ≈140 F g^{-1} but a poor rate performance due to the uncontrolled pore structure in graphene films. An additional thermal reduction step further complexed the fabrication process and affected the reversible extensibility of the substrate films.[15,16] Previous research demonstrated that CNT additives between graphene sheets could significantly improve the rate capability of printed graphene films by providing a more open and porous structure.[17] Although reduced graphene oxide (RGO) and CNT have been utilized in printable or stretchable SCs,[16,18] there is no report on the direct printing of highly stretchable SCs due to the limitation of printing techniques and available inks.

Here we present a facile, low-cost, and scalable approach to fabricate extremely stretchable and high-performance SCs based on 4D printing of composite electrodes using aerosol-jet printing technology and self-assembled origami. A new composition of RGO-CNT-poly(3,4-ethylenedioxythiophene) polystyrene sulfonate (PEDOT:PSS) solution as 3D printable precursor of flexible/extensible SC electrodes that exhibit cyclic deformability during and after printing of the conducting composite leading to 4D shape-morphable flexible electrode is reported in this article. The methanol solution mix from RGO-CNT-PEDOT:PSS is prepared and optimized as the ink to fabricate stretchable RGO-CNT-PEDOT:PSS-based SCs without an additional reduction process. The printed RGO-CNT-PEDOT:PSS composite films show excellent adhesion strength to the polymer substrate with CNTs and PEDOT:PSS (Clevios PH1000, Heraeus, Inc.) additives to significantly enhance the performance through increased conductivity and reduced restacking of RGO. The printed composite SCs can be charged at 5 A g^{-1}, with a specific capacitance of ≈20 F g^{-1} and a 85% capacitance retention from 0.5 to 5 A g^{-1} with large mechanical stretchability (i.e., 200% × 200%) through the design of RGO-CNT-PEDOT:PSS composite structure. A printed composite SC array (four in series) is further demonstrated to show the applicability and capability of the method for scalable building SC patterns with excellent electrochemical performance.

2. Results and Discussion

2.1. 4D Printing of Stretchable Composite Electrodes

Figure 1a illustrates the fabrication process of 4D printing of the stretchable hybrid RGO-CNT-PEDOT:PSS (PH1000) electrodes using an aerosol jet printer. A square-shaped optically clear acrylic substrate (VHB 4910, 3M, Inc.) was first stretched uniaxially in one direction or biaxially along two orthogonal in-plane directions using a biaxial stretcher developed in-house. The prestrains ε_{pre1} and ε_{pre2} can be adjusted based on the requirement in a range from 0% to 300%, thanks to the excellent stretchability of the substrate. The stretched polymer substrate dimensionally stabilized on the stretcher is then placed onto the platen to aerosol jet print the RGO-CNT-PEDOT:PSS inks on top of the substrate (Figure 1b) according to the designed electrode patterns. The RGO-CNT-PEDOT:PSS composite inks were prepared and characterized following the procedures in Experimental Section.[19] Previous study demonstrated that a hybrid composite of RGO:CNT with a ratio 1:1 can give superior performance as compared to other hybrid ratios.[20] The printability and the electrochemical performance, however, are not satisfactory for aerosol-jet printing and SC device fabrication due to the low viscoelasticity and low conductivity. To address this limitation, conducting polymer (PEDOT:PSS) solution was added to significantly enhance viscosity and printability of the mixed ink

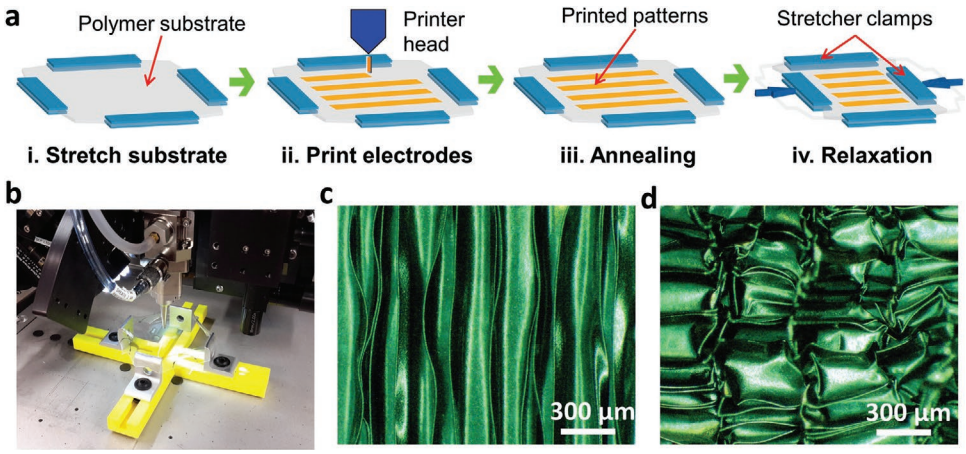

Figure 1. Fabrication of printed stretchable RGO-CNT-PH1000 electrode. a) Schematic illustration of the fabrication process for the 4D printing of a hybrid SC: i) stretch elastomer substrate; ii) print electrodes on the prestretched substrate; iii) annealing of the printed electrodes; and iv) relaxation of the elastomer substrate. b) Optical image of the 4D printing process by an aerosol jet printer. c,d) Optical microscopy of the origami pattern formed by the printed composite thin films on a fully relaxed elastomer substrate (i.e., 0% and 0% × 0% strain).

but also to drastically enhance the conductivity of the printed composite thin film. Figure S1, Supporting Information, shows the conductivity of the printed RGO-CNT-PEDOT:PSS films with different PEDOT:PSS concentrations. We find that 20 wt% PEDOT:PSS (i.e., PH1000) can yield the optimal performance in electrical conductivity and acceptable viscosity for aerosol-jet printing. As a result, in the following study, the composition of composite ink for electrode film printing is set to be 40 wt% RGO, 40 wt% CNT, and 20 wt % PH1000. During the printing process, an additional radiation heater was used to maintain the platen temperature at ≈60 °C to enhance the evaporation of the solvent from the printed film. After the printing of designed patterns (electrodes), the prestrains in the elastomer substrate were released to form the self-organized origami/ridge patterns due to the localized mechanical instabilities (Figure 1c,d)[3,21] As the prestrains in the extensible substrate were relaxed, the lateral size of the printed electrode film reduced by the same ratio as those of the substrate film. When the substrate is stretched back, the electrode unfolds reversibly, enabling extremely high stretchability of the hybrid electrode. The excellent toughness and flexibility of the printed composite electrode enable the high capacitance and good reliability of the stretchable device when subjected to multiple cycles of large deformations. It is noted that aerosol-jet printing of RGO-CNT-PH1000 can be applied to different substrates with shape-control ability. As shown in Figure S2, Supporting Information, the RGO-CNT-PH1000 composite films were successfully printed on different kinds of substrates such as the flexible Kapton film, aluminum (Al) sheet/foil, and stretchable acrylic substrates with complex patterns.

2.2. Characterization of the Materials and Printed Composite Films

The mechanical properties of the as-printed films on stretchable substrates were characterized experimentally. The stress–strain curve of the composite film was fitted well with a neo-Hookean model, giving a shear modulus of $\mu_f = 195$ MPa (Figure S3, Supporting Information). **Figure 2**a shows the scanning electron microscope (SEM) image of the surface morphology of a representative RGO-CNT-PH1000 composite on a Kapton substrate. It can be seen that in the composite film, CNTs directly contact with RGO sheets and act as a conductive network connecting discretized RGO nanosheets, which significantly improves the conductivity of the composite film. Figure 2b shows the nanostructures of the dense network of the printed CNT film, where the CNTs form a uniform nanotube network and many small nanogaps (interstitial space). The CNT network can increase the conductivity, robustness, and electron transfer rate of the composite electrode while the nanogaps in the CNT networks allow fast ion transport inside the composite, leading to improved rate capability of printed SCs. Figure 2c–f illustrates the transmission electron microscope (TEM) images of the composite films. The RGO, CNT, and PH1000 were well mixed in the composite film due to strong van der Waals attraction. The CNT networks between individual RGO nanosheets reduced the likelihood of RGO flakes stacking/aggregation in the deposition process, resulting in increased accessible surface area, which led to high specific capacitance, high energy density, and power density.[17,22]

Figure S4a, Supporting Information, depicts the Raman spectroscopy and the X-ray photoelectron spectroscopy (XPS) of the CNT, RGO, PH1000, and composite films. For PH1000, the main peak (C=C symmetric stretching in Thiophene plane mode) at 1433 cm corresponds well to previous literature reports.[23] The 1262 cm band is attributed to the inter ring C_α–$C_{\alpha'}$ stretching. The 1367 cm band is caused by the C_β–C_β stretching mode in the Thiophene ring. The 1560 cm band is attributed to the C=C asymmetric stretching vibration in thiophene plane.[23] For RGO, three prominent peaks were observed at 1323 (D band), 1573 (G band), and 1600 cm (D′ band). The 2.25 D/G ratio indicates small, numerous in-plane sp^2 domains created by the reduction of graphene oxide.[24] Note that because the relative Raman intensity of RGO is small,

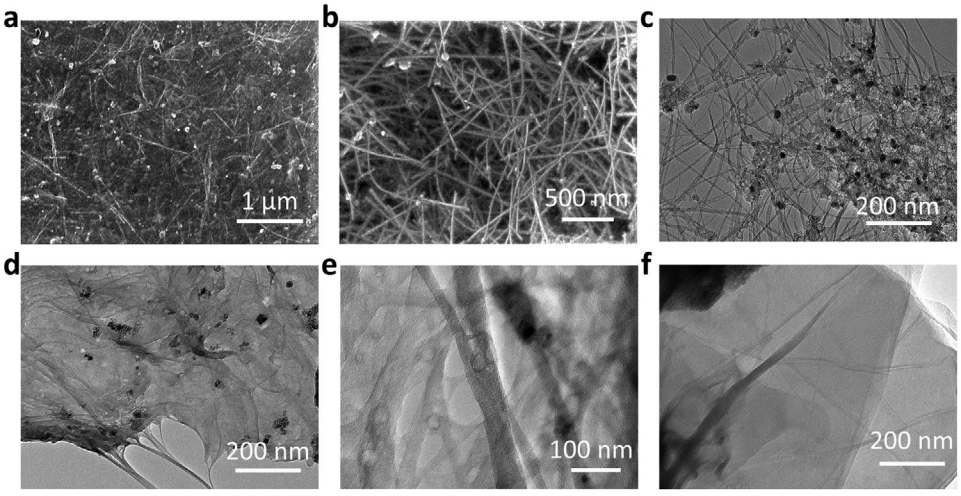

Figure 2. Morphologies and dispersion of the nanocomposite films made of RGO, CNT, and PH1000. a) SEM image of the top view of a composite film. b) SEM image of the top view of the CNT network. c) TEM images of the RGO-CNT film. d) TEM image shows the uniform dispersion of the PEDOT:PSS in a composite film. e) TEM image of the RGO-CNT-PH1000 film. f) TEM image of the composite film with the strong interaction of RGO sheets/flakes and CNTs.

the Raman intensity of RGO is multiplied by 30 for a clearer spectra. For CNTs, the small 1325 cm D band and large 1581 cm G band indicate a low concentration of defects and large in-plane sp^2 domains. The structural integrity provides high conductivity and low resistance when the CNTs are included as a component of the ink. The G′ band around 2617 cm for CNTs is attributed to the second-order two phonon process.[25] For the RGO-CNT-PH1000 composite, the signature peaks of PH1000 and CNT are easily recognized while RGO peaks are hard to observe due to their relatively low Raman intensity. The XPS scan of the RGO-CNT-PH1000 composite film is shown in Figure S4b, Supporting Information. The S and Na peaks confirm the PH1000 polymer on the surface that indicate the uniformity of the composite. The low concentrations of F and N detected in the survey scan may be attributed to the surface groups remained during the synthesis of CNT and RGO. The region scans of S and C are shown in Figure S4c,d, Supporting Information, respectively. S peak envelop in Figure S4c, Supporting Information, can be deconvolved into four separate peaks. The 164.2 and 165.2 eV peaks are attributed to the thiophene groups in PEDOT. The 168.1 and 169.2 eV peaks are due to the sulfonate groups in PSS.[26] The C peak envelop is deconvolved into three peaks: C—C, C—O, and C=O (Figure S4d, Supporting Information). The C—O peak contribution comes from the ethylenedioxy groups in PH1000 and oxygen functional groups in CNT and RGO. The C=O peak is mainly attributed to the carboxyl groups in RGO and CNT.

2.3. Electrochemical Performance of Printed Composite Electrodes

To demonstrate the stretchability and performance of the printed hybrid RGO-CNT-PH1000 electrodes, we characterized the cyclic voltammetry (CV), electrochemical impedance spectroscopy (EIS), and galvanostatic charge/discharge (GCD) behaviors of biaxial stretchable electrodes in 2 M KCl electrolyte. Figure S5a, Supporting Information, shows the CV curves of the stretchable SC measured at different scan rates ranging from 20 to 100 mV s^{-1} under relaxed (0% × 0% strain) state. The near-rectangular curves indicate the electrochemical double layer (EDL) behavior and small resistance of the electrode. Experimental data showed that the CV curves retained a rectangular shape with ideal capacitive behavior even at a high scan rate of 100 mV s^{-1}, indicating good capacitive behavior and rapid diffusion and transportation of the electrolyte ions from the electrolyte to the pores of the electrode materials. Such a good electrochemical performance is mainly attributed to the improved conductivity of the composite and little restacking of RGO flakes. Figure S5b, Supporting Information, compares the CV of RGO-CNT-PH1000 under different strains (i.e., 0% × 0% and 200% × 200%) at the scan rate of 50 mV s^{-1}. The almost identical CV curves at different strained states (e.g., both extended and folded structure as displayed in Figure 1c,d) indicate that RGO-CNT-PH1000 film retained similar capacitance even under extreme mechanical deformations. The consistent electrochemical performance of the stretchable electrode is also confirmed by the EIS curves (Figure S5c, Supporting Information) in which the composite electrode under different strain states exhibits similar charge transfer resistance features in the semicircle of high-frequency range and near-vertical slope in low-frequency range, indicating the excellent electrochemical behavior of the RGO-CNT-PH1000 electrode. Figure S5d, Supporting Information, presents the GCD curves of the composite electrode measured at different current densities under different strains. The charge/discharge time of the electrodes is almost the same under different strain states at all tested current densities. Particularly, as shown in in Figure S5e, Supporting Information, ten GCD cycles of the composite electrode at 1 A g^{-1} under different strain states are compared, demonstrated identical charge/discharge behaviors in a longer time scale (i.e., 10 cycles). Figure S5f, Supporting Information, presents the specific capacitance of the printed composite electrode calculated from the GCD measurements. The printed electrodes have an excellent gravimetric capacitance in the range of 95–105 F g^{-1} at the current density from 0.5 to 5 A g^{-1}. The high capacitance retention (≈90%) and identical capacitance at different strain states are ascribed to the unique structure of the composite with CNT-PH1000 conductive network for improved conductivity and little restacking of RGO flakes.

To demonstrate the versatile applications of aerosol-jet printing on different substrates, the electrochemical performance of the RGO-CNT-PH1000 composite film on a flexible but not that extensible polyimide (Kapton) film was also tested (Figure S6, Supporting Information). Compared to the composite electrodes on a stretchable elastomer substrate, the electrode on the Kapton film demonstrated a higher capacitance evidenced by the larger current density of the CV (Figure S6a, Supporting Information) and longer charge/discharge time of GCD measurements at the same current density (Figure S6b, Supporting Information). Figure S6c, Supporting Information, shows the EIS curve of the RGO-CNT-PH1000 composite electrode on the Kapton film. The curve shows a similar semicircle in the high-frequency region but less vertical slope in the low-frequency region compared to the composite on the stretchable elastomer substrate. The observed difference in the EIS curves agrees well with the more distorted CV shape at higher scan rates (Figure S6a, Supporting Information), likely due to the different composite microstructure formed on different substrates. Generally, the RGO-CNT-PH1000 electrode on a Kapton film demonstrated a superior specific capacitance of 162.5 F g^{-1} at a low current density (e.g., 0.5 A g^{-1}) but an inferior capacitance retention (≈61%) from 0.5 to 5 A g^{-1}, as shown in Figure S6d, Supporting Information.

2.4. Electrochemical Performance of All-Solid-State SCs

All-solid-state SCs were fabricated by assembling two printed stretchable composite electrodes with PVA-KCl gel electrolyte. The fabrication process for a symmetric SC is illustrated in **Figure 3**a. In brief, the as-prepared prestrained composite electrode was cast-coated with a thin layer of PVA-KCl and then dried in a fume hood. The electrodes were then connected with Pt wires (current collectors) and assembled in the prestrained state. The assembled device was finally relaxed to form a self-assembled origami/ridge pattern. Figure 3b presents the CV curves of the SC at different scan rates under a strain of

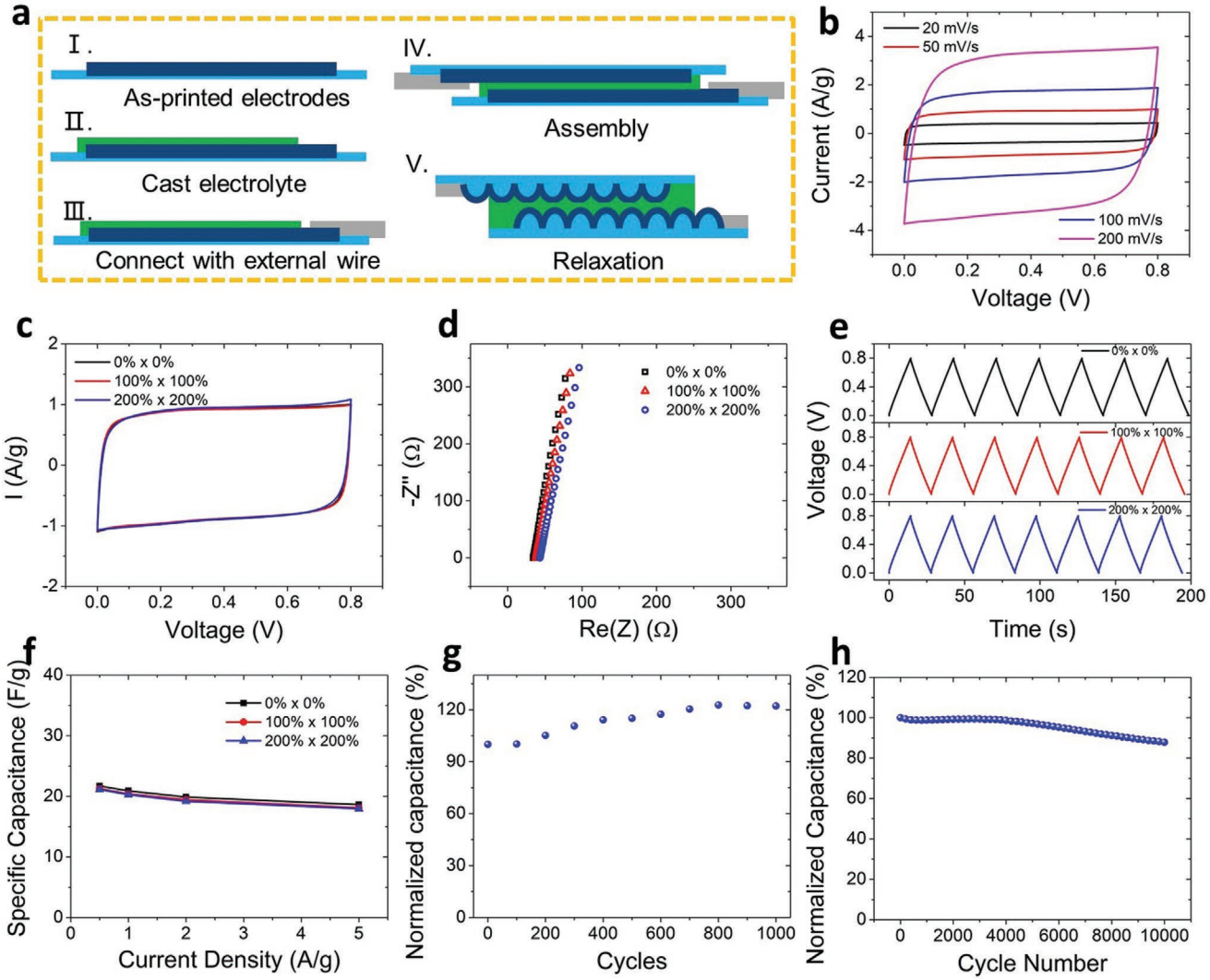

Figure 3. Electrochemical performance of a biaxially stretchable SC printed by an aerosol jet printer. a) Schematic illustration of the fabrication process of 4D printing of a stretchable symmetric SC. b) CV curves of the stretchable SC at different scan rates at the stretched strain of 100% × 100%. c) CV curves of the stretchable SC at 50 mV s^{-1} at different strain states (0% × 0%, 100% × 100%, and 200% × 200%). d) Nyquist plot of the RGO-CNT-PH1000 composite electrode at 0 V at different strain states (0% × 0%, 100% × 100%, and 200% × 200%). e) GCD curves of the stretchable SC at 1 A g^{-1} at different strain states (0% × 0%, 100% × 100%, and 200% × 200%). f) Specific capacitance of the stretchable SC at different current densities at different strain states (0% × 0%, 100% × 100%, and 200% × 200%). g) Mechanical stability of the hybrid composite SC under 150% uniaxial tensile strain. The capacitance increased by 20% after 1000 cycles. h) Electrochemical stability of the SC at 1 A g^{-1}. The capacitance retention is ≈88% after 10 000 cycles.

100% × 100%. Similar to the printed electrodes, the SC demonstrates a square-like shape at different scan rates from 20 to 200 mV s^{-1}. Figure 3c shows the CV curves of the SC at different strain states are almost identical, indicating constant electrochemical performance of the device when subjected to large deformations. As shown in Figure 3d, EIS curves of the stretchable SC at three different strain states are similar, showing a low series resistance in the range of 35–45 Ω. The charge transfer resistance is also small and almost no semicircle in high-mid-frequency range (i.e., from 200 kHz to 10 Hz) is observed. The small charge transfer resistance of the SC is attributed to the better ionic and electric conductivity, owing to the optimized nanostructure and conductivity of the composite electrodes. Figure 3e presents the GCD curves of SC at 1 A g^{-1} at different strain states. The triangular shape of the GCD curves agrees with CV measurements in Figure 3b, which indicates the major contribution comes from EDL capacitance in the composite electrodes. The charge/discharge time of one cycle at 1 A g^{-1} at strain state of 0% × 0%, 100% × 100%, and 200% × 200% is measured to be 28.36, 27.97, and 27.74 s, respectively. Figure 3f shows the specific capacitances calculated from the GCD measurements at different current densities and different strain states. The stretchable SC demonstrated a specific capacitance of ≈ 21 F g^{-1} at 0.5 A g^{-1} and a capacitance retention of ≈85% from 0.5 to 5 A g^{-1} at all strain states, resulting from the superior conductivity and mechanical robustness of the composite electrodes. Since a symmetric SC should have a capacitance of one-fourth of a single electrode capacitance, the observed smaller SC capacitance may be due to different capacitances for individual electrodes and/or an electrolyte ion effect.

The KCl electrolyte is known to yield a lower capacitance than the ideal case but it is safer than the acid-based electrolytes.

Figure 3g shows the capacitance of the printed SC as a function of the stretching–relaxation cycle number with an applied uniaxial strain up to 150%. A slight increase of ≈20% of its initial capacitance (i.e., the capacitance before mechanical stretching–relaxation cycles) was observed after 1000 stretching–relaxation cycles. The EIS spectra were also recorded to analyze the effect of cyclic mechanical deformation on the electrochemical performance of the composite SC (Figure S7a, Supporting Information). As shown in the Nyquist plots in Figure S7a, Supporting Information, the composite SC shows a similar behavior in the high-frequency semicircle zone before and after performing multiple cycles of stretching–relaxation. The diameter of the semicircle is related to the charge transfer resistance R_{CT} at the interface of the RGO-CNT-PH1000 electrodes and electrolyte as well as the resistance within the pores. As illustrated in the inset of Figure S7a, Supporting Information, the extracted R_{CT} remains low during the 1000 stretching–relaxation cycles, indicating that the cyclic large strains did not significantly affect the transfer resistance of the stretchable electrodes or result in a reduction in the performance of the stretchable electrodes. Figure S7b, Supporting Information, shows the CV curves of the SC after every 200 mechanical cycles. It can be seen that the capacitance of the SC increased slightly after 1000 cycles of mechanical stretching–relaxation, which is believed to be due to the better interface contacts and the porous structure in the electrodes induced by the large cyclic mechanical strains. Figure 3h illustrates the excellent electrochemical stability of the stretchable SC subjected to multiple cycles of electromechanical loadings. It can be seen that an 88% capacitance retention can be achieved after 10 000 GCD cycles at a scan rate of 1 A g^{-1}.

The stretchable SC can be printed onto different kinds of substrates with a controllable shape for scalable manufacturing. To demonstrate this, a SC array made of four trapezoid SCs connected in series was printed on a Kapton film and assembled with PVA-H_3PO_4 gel electrode. It is reported that H_3PO_4 gel-electrolyte can yield the best electrochemical performance for graphene SCs.[27] As shown in **Figure 4**a, each SC of the flexible SC array is connected by conductive metal lines (can be printed or sputter-coated) to achieve low resistance of the whole device. The SC array has a potential window of 3.2 V after serially connecting four SCs. Figure 4b shows the CV curves of the SC array at different scan rates from 20 to 1000 mV s^{-1}. The CV curves remained a rectangular shape even at 1000 mV s^{-1}, indicating excellent rate capability enabled by the good electrode conductivity and easy transportation of ions. The outstanding electrochemical performance is also confirmed by the GCD curves of the SC array at different current densities with small ohmic drop and ideal triangular shape (Figure 4c). Remarkably, the SC array on the flexible Kapton substrate can maintain its capacitance when bent to different radius (Figure 4d). Figure 4e,f depicts the CV curves (measured at 100 mV s^{-1}) and GCD curves (obtained at 10 μA cm^{-2}) of a single SC and a SC array consisting of four SCs. It can be seen that the current of the single device is approximately four times higher than the SC array, agreeing very well with the theoretical prediction. Additionally, the charge/discharge time of an individual device from 0 to 0.8 V is similar to that of the SC array device from 0 to 3.2 V (Figure 4f), confirming an approximately one-fourth capacitance relationship. The good agreement between the experimental results and the theoretical calculation is mainly attributed to the accurate material control in the aerosol-jet printing process, which is vital for scalable manufacturing for the large-scale fabrications. Figure 4g presents the self-discharge and leakage current measurement of a single SC device. The leakage current is observed to be 2 μA after 12 h charging. The voltage of the SC drops to 50% of its original value after ≈0.5 h in the subsequent self-discharge measurement. The moderate self-discharge time of the RGO-CNT-PH1000 SC may be attributed to the high defect density of RGO (Figure S3, Supporting Information) which can serve as leakage paths in the SC electrode. To demonstrate the practical application of the printed stretchable SC, the flexible in-series SC array is demonstrated to lighten a single LED and a LED array (Figure 4h,i) successfully for a few seconds (Figures S8 and S9, Supporting Information).

The specific capacitance and stretchability of the printed electrodes and SCs are compared with other printed RGO/CNT-based electrodes/SCs reported in literature (**Figure 5**). It can be seen from Figure 5a that the proposed RGO-CNT-PH1000 composite electrodes demonstrate comparable capacitance and much higher stretchability than other reported results. In the aspect of stretchability, previous printed RGO or CNT was mainly fabricated on rigid or flexible substrate that limits their potential applications in wearables and other stretchable electronic systems. As for the electrochemical performance, printed RGO electrodes give a smaller capacitance especially at high charge/discharge rates than the RGO-CNT-PH1000 electrodes, which may be due to the unoptimized micro/nanostructure. Compared to the RGO-CNT-PH1000 composite electrode, printed CNT electrodes yielded a lower capacitance owing to their smaller specific surface area. The combination of considerable capacitance, excellent rate capability, and extreme stretchability with a 4D printing fabrication process is unique and facile for fabricating high-performance robust stretchable electrodes and SCs. Figure 5b demonstrates the performance of the different kinds of SCs reported in literature. Similarly, the RGO-CNT-PH1000 SC shows analogous capacitance with excellent mechanical reliability, which is promising for future wearable/stretchable energy storage devices fabricated in a cheap and scalable way. More detailed performance comparison of the composite electrodes/SCs with other results reported in literature is listed in Tables S1 and S2, respectively, Supporting Information.

3. Conclusion

In summary, we have demonstrated a facile, low-cost, efficient, scalable, and shape-controlled approach to fabricate stretchable SCs by combining 4D printing techniques with self-organized origami patterns. The printed composite electrodes made of RGO, CNT, and conducting polymer demonstrated excellent electrochemical performance and mechanical reliability

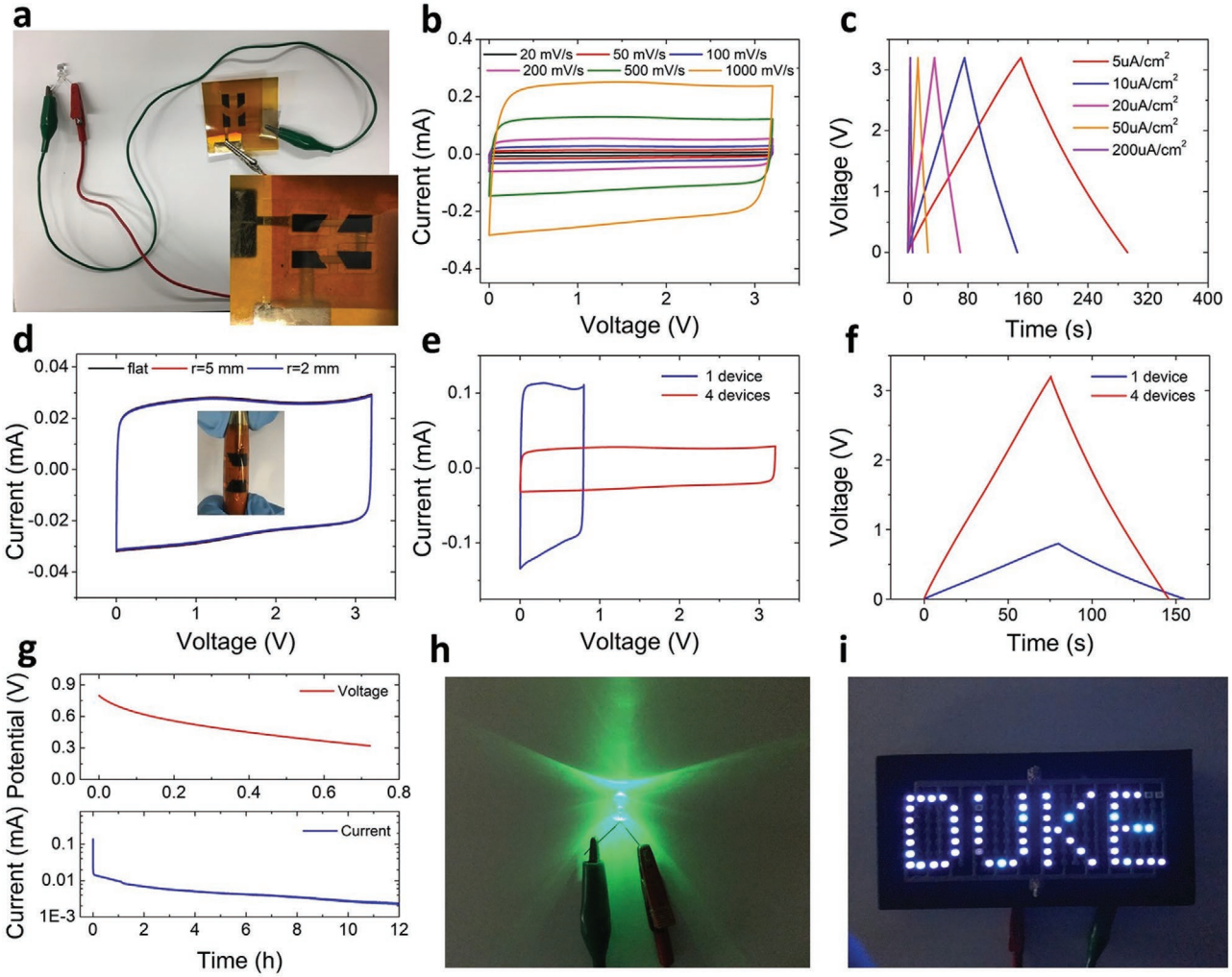

Figure 4. Electrochemical performance and demonstration of a flexible SC array. a) Optical images of an assembled RGO-CNT-PEDOT SC (four in series). b) CV curves of the RGO-CNT-PEDOT SC array from 20 to 1000 mV s^{-1}. c) GCD curves of the RGO-CNT-PEDOT SC array with different current densities from 5 to 200 μA cm^{-2}. d) The CV curves of the printed flexible SC array when bended to different curvature radii. Inset: Photograph of the printed SC array bended by wrapping around a cylinder with a curvature radius of 5 mm. The scan rate is 100 mV s^{-1}. e) Comparison of the CV curves of a single SC and four serially connected SCs at 100 mV s^{-1}. f) Comparison of the GCD curves of a single SC and four serially connected SCs at 10 μA cm^{-2}. g) Leakage current and self-discharge characterizations for a single trapezoid stretchable SC. h,i) The four SCs connected in series can be used to power a green LED or a LED array.

under extremely large strains. With a polymer hydrogel electrolyte, we also fabricated high-performance all-solid state stretchable SCs, exhibiting an identical specific capacitance of 21.7 F g^{-1} at 0.5 A g^{-1} and a capacitance retention of ≈85.8% from 0.5 to 5 A g^{-1} under large biaxial strains (i.e., 100% × 100% and 200% × 200%). Moreover, the 4D printed SCs can maintain high electrochemical performance and functionality under large cyclic mechanical deformations. A printed trapezoid SC array with extended voltage range and considerable electrochemical performance was further fabricated to demonstrate the universal applicability, scalability, and shape-control ability of 4D printing of stretchable SC devices. The developed strategy can be extended to other responsive/smart materials and paves a new avenue for fabricating programmable structures and electronics devices. The 4D printing strategy will become an attractive method for fabricating future advanced energy-storage devices and next-generation power-independent stretchable electronic systems for a variety of applications.

4. Experimental Section

Composite Ink Synthesis: RGO (Carbon Solutions, Inc., USA) was prepared by borohydride reduction of graphene oxide (Hummer's method). Purified SWCNTs (P3-SWCNT, Carbon Solutions, Inc., USA) was produced by electric arc method and were dispersed in distilled water by sonication and washed intensively with NaOH solution to remove carboxylated carbon fragments. The obtained CNT powder and RGO powder were, respectively, dispersed in methanol to a concentration of 0.5 mg mL^{-1}, and then mixed thoroughly with a ratio of 1:1, followed by ultrasonication for 20 min. To improve the printability of the ink and to enhance the conductivity of the printed hybrid film, 5–20 vol% of conducting polymer PEDOT:PSS (Clevios PH1000, Heraeus, Inc.) was added. In addition, 9% of DMSO was added into

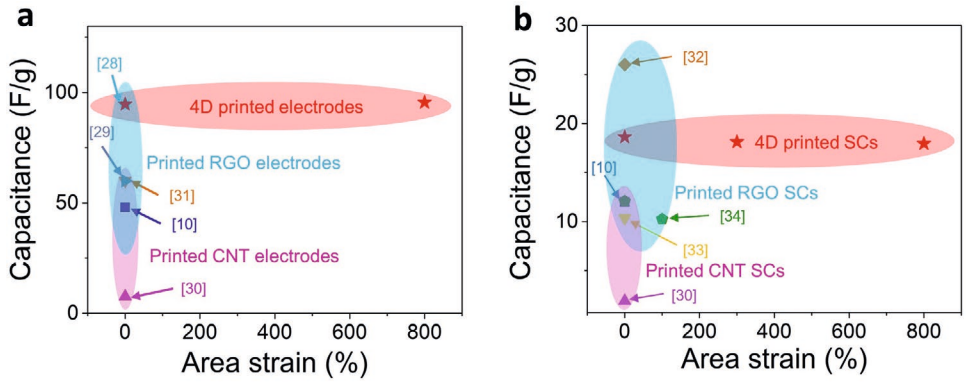

Figure 5. Comparison of the capacitance and stretchability between the printed RGO-CNT-PH1000 electrode and SC with other printed or stretchable RGO/CNT electrodes and SCs. a) Electrode comparison: red star—RGO-CNT-PH1000 presented in this work, blue square—inkjet-printed RGO,[10] cyan circle—printed RGO with leavening agent,[28] dark cyan right triangle—3D printed RGO,[29] magenta upper triangle—printed CNT,[30] orange down triangle—printed CNT fabric.[31] b) SC comparison: red star—RGO-CNT-PH1000 in this work, blue square—inkjet-printed RGO,[10] orange diamond—printed nano-graphene platelets (NGP),[32] magenta upper triangle—printed CNT,[30] yellow down triangle—printed RGO-CNT,[33] green pentagon—printed stretchable graphene composite.[34]

the PEDOT:PSS solution to enhance its conductivity. The resulting ink obtained was aerosol jet printed on a variety of substrates such as the polyimide films, silicon wafers, glass slides, and metal sheets.

Material Characterization: The electrode materials were characterized by optical microscopy, SEM, TEM, Raman, and XPS measurements. Optical image was taken by a Zeiss Axio Lab microscope configured with 2.5× to 100× objective lenses and a digital camera for image capture and analysis. The morphology and microstructures of ink materials and printed composite were acquired with FEI XL30 (SEM-FEG, USA) with varied magnifications. TEM imaging was performed using a TEM system (FEI Tecnai G2 Twin). Raman spectroscopy was performed for the CNT, RGO, PH1000, and RGO-CNT-PH1000 composites using a Horiba Jobin Yvon LabRAM ARAMIS system, with a 633 nm laser used as the excitation light. Surface compositions of the CNT, RGO, PH1000, and RGO-CNT-PH1000 composite thin films were characterized by XPS using a Kratos Analytical Axis Ultra system with an Al Kα monochromated X-ray source. Vacuum pressure was kept around 2×10^{-8} Torr during the acquisition. XPS data were analyzed and deconvoluted by a CasaXPS software. The sheet resistance of the printed electrodes was measured by 4200-SCS semiconductor characterization system.

Printing Fabrication of the Composite Electrodes: All printing work was done using an aerosol jet printer (Optomec, Inc.) operated in air at room temperature. The printing was conducted on various substrates including extensible acrylic tape, Kapton film, and Al foil/sheet. The stage was heated to 80 °C for all printing steps to facilitate solvent evaporation. A circular wide nozzle (diameter of 1.5 mm) was used for the printing, and the carrier gas (N_2) and sheath gas (N_2) flow rates are 50 and 100 sccm, respectively. Stage speed was set to be 5–10 mm s^{-1}. All printing steps were carried out in air at room temperature while the platen was maintained at 80 °C to enhance ink drying. Three layers of RGO-CNT-PH1000 were printed with the second layer using a print direction orthogonal to the first and third layers to improve uniformity. The printed samples were further annealed at 100 °C for 30 min in oven (MDL 281, Thermo Fisher Scientific).

Fabrication of All-Solid-State Flexible SCs: PVA-H_3PO_4 was chosen as the solid-state electrolyte for flexible SCs, with four SCs connected in series. A total of 2.5 g of poly(vinyl alcohol) (PVA) was dissolved into 25 mL deionized water. The solution was heated to 90 °C and stirred for 1 h until it became clear. A total of 0.2 mL of 85 wt% H_3PO_4 was then added into the solution and stirred for another 15 min. The as-prepared PVA-H_3PO_4 electrolyte was degassed in a vacuum chamber. To fabricate tandem CNT-RGO-PEDOT solid-state SCs, the PVA-H_3PO_4 electrolyte was first drop cast on a Teflon mold and dried overnight to obtain a PVA-H_3PO_4 thin film. The PVA-H_3PO_4 thin film was then submerged in 85% weight ratio phosphoric acid (J. B. Baker) solution for 30 min before its use. Two printed composite electrodes and the PVA-H_3PO_4 electrolyte were then assembled together to form a symmetric double-layer SC. The PVA-H_3PO_4 gel serves as a separator and the solid-state-electrolyte layer. Finally, the CNT-RGO-PH1000 solid-state SC was tested as a standard two-electrode system.

Fabrication of All-Solid-State Stretchable SCs: The all-solid-state stretchable SC was assembled with two 4D printed composite electrodes and the PVA-KCl gel electrolyte. First, PVA gel electrolyte was prepared as follows: 2.5 g of PVA was dissolved into 25 mL deionized water. The solution was heated to 90 °C under vigorous stirring for about 1 h until it became clear. Then, 3 g KCl (VWR Analytical) was added into the solution and stirred for 10 min. After cooling down, the solution was degassed in a vacuum chamber to get rid of the bubbles. To make the solid-state SC, the PVA-KCl solution was drop cast onto the stretchable electrode with a biaxial prestrain of 200% × 200%. Pt wires were connected with the printed electrode film for current collecting. After drying for 30 min in air, the two prestretched electrodes were laminated together and dried on an 80 °C hotplate for 10 min. The assembly was carried out in a fume hood at the room temperature. The assembled device was finally mounted on a custom-made stage for testing using a standard two-electrode configuration under different applied strains.

Electrochemical Measurements of Printed Stretchable Electrodes and SCs: CV, GCD, and EIS of the electrodes and SCs were measured with a Potentiostat (Bio-Logic SP-300). The printed composite electrodes were characterized using a standard three-electrode setup in a 2 M KCl solution. The printed electrode served as the working electrode, a platinum wire as the counter electrode, and an Ag/AgCl electrode in saturated KCl as the reference electrode. The scan rate of CV was varied from 20 to 200 mV s^{-1}. The all-solid-state stretchable SCs were characterized with a standard two-electrode system. After mounted on an in-house developed stage, the electrochemical measurements for the SC were carried out under various strains. The CV and GCD of the stretchable SCs were tested in an operation voltage range from 0 to 0.8 V. The current density was varied from 0.5 to 5 A g^{-1}. A total of 10 000 GCD cycles at 1 A g^{-1} were used to test the electrochemical stability. EIS was conducted at open circuit potential over the frequency range from 200 kHz to 100 mHz with a sinusoidal potential amplitude of 10 mV. For the composite SC, EIS was performed after fixing the voltage at 0 V for 2 min. The capacitances are calculated based on the mass of the carbon materials used in the electrodes and the SCs. The specific capacitance was calculated from the slope of the discharge curve. Constant current charge/discharge tests were performed in the range of 5–200 μA cm^{-2} for the all-solid-state SCs.

Supporting Information

Supporting Information is available from the Wiley Online Library or from the author.

Acknowledgements

This work is partially supported by NSF (ECCS-2024649), NSF (ECCS-1344745), USDA-NIFA (Hatch Project-1016788), and Michigan State University. The authors thank Dr. Aaron Franklin, Dr. Shengrong Ye, and Dr. Patrick Flowers from Duke University for the helpful discussion and assistance in the initial printing tests and the LED demonstration.

Conflict of Interest

The authors declare no conflict of interest.

Keywords

4D printing, aerosol-jet printing, hybrid composites, self-organized origami, stretchable supercapacitors

Received: October 28, 2020
Published online:

[1] a) D.-H. Kim, J.-H. Ahn, W. M. Choi, H.-S. Kim, T.-H. Kim, J. Song, Y. Y. Huang, Z. Liu, C. Lu, J. A. Rogers, *Science* **2008**, *320*, 507; b) L. Xiao, Z. Chen, C. Feng, L. Liu, Z.-Q. Bai, Y. Wang, L. Qian, Y. Zhang, Q. Li, K. Jiang, S. Fan, *Nano Lett.* **2008**, *8*, 4539; c) S.-K. Lee, B. J. Kim, H. Jang, S. C. Yoon, C. Lee, B. H. Hong, J. A. Rogers, J. H. Cho, J.-H. Ahn, *Nano Lett.* **2011**, *11*, 4642; d) S. C. B. Mannsfeld, B. C. K. Tee, R. M. Stoltenberg, C. V. H. H. Chen, S. Barman, B. V. O. Muir, A. N. Sokolov, C. Reese, Z. Bao, *Nat. Mater.* **2010**, *9*, 859.

[2] D. J. Lipomi, M. Vosgueritchian, B. C. K. Tee, S. L. Hellstrom, J. A. Lee, C. H. Fox, Z. Bao, *Nat. Nanotechnol.* **2011**, *6*, 788.

[3] C. C. Fu, A. Grimes, M. Long, C. G. L. Ferri, B. D. Rich, S. Ghosh, S. Ghosh, L. P. Lee, A. Gopinathan, M. Khine, *Adv. Mater.* **2009**, *21*, 4472.

[4] D.-H. Kim, N. Lu, R. Ma, Y.-S. Kim, R.-H. Kim, S. Wang, J. Wu, S. M. Won, H. Tao, A. Islam, K. J. Yu, T.-i. Kim, R. Chowdhury, M. Ying, L. Xu, M. Li, H.-J. Chung, H. Keum, M. McCormick, P. Liu, Y.-W. Zhang, F. G. Omenetto, Y. Huang, T. Coleman, J. A. Rogers, *Science* **2011**, *333*, 838.

[5] a) S. Wagner, S. Bauer, *MRS Bull.* **2012**, *37*, 207; b) J. A. Rogers, T. Someya, Y. Huang, *Science* **2010**, *327*, 1603; c) M. Kaltenbrunner, M. S. White, E. D. Głowacki, T. Sekitani, T. Someya, N. S. Sariciftci, S. Bauer, *Nat. Commun.* **2012**, *3*, 770; d) D.-Y. Khang, H. Jiang, Y. Huang, J. A. Rogers, *Science* **2006**, *311*, 208; e) C. Keplinger, J.-Y. Sun, C. C. Foo, P. Rothemund, G. M. Whitesides, Z. Suo, *Science* **2013**, *341*, 984; f) D. J. Lipomi, B. C. K. Tee, M. Vosgueritchian, Z. Bao, *Adv. Mater.* **2011**, *23*, 1771.

[6] S. Xu, Y. Zhang, J. Cho, J. Lee, X. Huang, L. Jia, J. A. Fan, Y. Su, J. Su, H. Zhang, H. Cheng, B. Lu, C. Yu, C. Chuang, T.-i. Kim, T. Song, K. Shigeta, S. Kang, C. Dagdeviren, I. Petrov, P. V. Braun, Y. Huang, U. Paik, J. A. Rogers, *Nat. Commun.* **2013**, *4*, 1543.

[7] Z. Song, T. Ma, R. Tang, Q. Cheng, X. Wang, D. Krishnaraju, R. Panat, C. K. Chan, H. Yu, H. Jiang, *Nat. Commun.* **2014**, *5*, 3140.

[8] a) X. Li, T. Gu, B. Wei, *Nano Lett.* **2012**, *12*, 6366; b) L. Hu, M. Pasta, F. L. Mantia, L. Cui, S. Jeong, H. D. Deshazer, J. W. Choi, S. M. Han, Y. Cui, *Nano Lett.* **2010**, *10*, 708; c) Z. Yang, J. Deng, X. Chen, J. Ren, H. Peng, *Angew. Chem., Int. Ed.* **2013**, *52*, 13453; d) V. L. Pushparaj, M. M. Shaijumon, A. Kumar, S. Murugesan, L. Ci, R. Vajtai, R. J. Linhardt, O. Nalamasu, P. M. Ajayan, *Proc. Natl. Acad. Sci. USA* **2007**, *104*, 13574; e) C. Liu, Z. Yu, D. Neff, A. Zhamu, B. Z. Jang, *Nano Lett.* **2010**, *10*, 4863; f) Y. Zhu, S. Murali, M. D. Stoller, K. J. Ganesh, W. Cai, P. J. Ferreira, A. Pirkle, R. M. Wallace, K. A. Cychosz, M. Thommes, D. Su, E. A. Stach, R. S. Ruoff, *Science* **2011**, *332*, 1537; g) J. R. Miller, R. A. Outlaw, B. C. Holloway, *Science* **2010**, *329*, 1637.

[9] a) Y. Huang, M. Zhong, F. Shi, X. Liu, Z. Tang, Y. Wang, Y. Huang, H. Hou, X. Xie, *Angew. Chem., Int. Ed.* **2017**, *56*, 9141; b) Y. Huang, M. Zhong, Y. Huang, M. Zhu, Z. Pei, Z. Wang, Q. Xue, X. Xie, C. Zhi, *Nat. Commun.* **2015**, *6*, 10310; c) H. Li, T. Lv, H. Sun, G. Qian, N. Li, Y. Yao, T. Chen, *Nat. Commun.* **2019**, *10*, 536.

[10] L. T. Le, M. H. Ervin, H. Qiu, B. E. Fuchs, W. Y. Lee, *Electrochem. Commun.* **2011**, *13*, 355.

[11] J. Li, F. Ye, S. Vaziri, M. Muhammed, M. C. Lemme, M. Östling, *Adv. Mater.* **2013**, *25*, 3985.

[12] L. Huang, Y. Huang, J. Liang, X. Wan, Y. Chen, *Nano Res.* **2011**, *4*, 675.

[13] F. Torrisi, T. Hasan, W. Wu, Z. Sun, A. Lombardo, T. S. Kulmala, G.-W. Hsieh, S. Jung, F. Bonaccorso, P. J. Paul, *ACS Nano* **2012**, *6*, 2992.

[14] K. Kordás, T. Mustonen, G. Tóth, H. Jantunen, M. Lajunen, C. Soldano, S. Talapatra, S. Kar, R. Vajtai, P. M. Ajayan, *Small* **2006**, *2*, 1021.

[15] C. Cao, Y. Feng, J. Zang, G. P. López, X. Zhao, *Extreme Mech. Lett.* **2015**, *4*, 18.

[16] J. Zang, C. Cao, Y. Feng, J. Liu, X. Zhao, *Sci. Rep.* **2014**, *4*, 6492.

[17] M. Beidaghi, C. Wang, *Adv. Funct. Mater.* **2012**, *22*, 4501.

[18] a) C. Cao, Y. Zhou, S. Ubnoske, J. Zang, Y. Cao, P. Henry, C. B. Parker, J. T. Glass, *Adv. Energy Mater.* **2019**, *9*, 1900618; b) Y. Zhou, C. Cao, Y. Cao, Q. Han, C. B. Parker, J. T. Glass, *Matter* **2020**, *2*, 1307; c) C. Cao, Y. Chu, Y. Zhou, C. Zhang, S. Qu, *Small* **2018**, *14*, 1803976.

[19] a) D. A. Dikin, S. Stankovich, E. J. Zimney, R. D. Piner, G. H. Dommett, G. Evmenenko, S. T. Nguyen, R. S. Ruoff, *Nature* **2007**, *448*, 457; b) X. Yang, C. Cheng, Y. Wang, L. Qiu, D. Li, *Science* **2013**, *341*, 534.

[20] N. Jha, P. Ramesh, E. Bekyarova, M. E. Itkis, R. C. Haddon, *Adv. Energy Mater.* **2012**, *2*, 438.

[21] a) J. Zang, S. Ryu, N. Pugno, Q. Wang, Q. Tu, M. J. Buehler, X. Zhao, *Nat. Mater.* **2013**, *12*, 321; b) C. Cao, H. F. Chan, J. Zang, K. W. Leong, X. Zhao, *Adv. Mater.* **2014**, *26*, 1763.

[22] Z.-D. Huang, B. Zhang, S.-W. Oh, Q.-B. Zheng, X.-Y. Lin, N. Yousefi, J.-K. Kim, *J. Mater. Chem.* **2012**, *22*, 3591.

[23] F. Tran-Van, S. Garreau, G. Louarn, G. Froyer, C. Chevrot, *J. Mater. Chem.* **2001**, *11*, 1378.

[24] S. Stankovich, D. A. Dikin, R. D. Piner, K. A. Kohlhaas, A. Kleinhammes, Y. Jia, Y. Wu, S. T. Nguyen, R. S. Ruoff, *Carbon* **2007**, *45*, 1558.

[25] H. M. Heise, R. Kuckuk, A. K. Ojha, A. Srivastava, V. Srivastava, B. P. Asthana, *J. Raman Spectrosc.* **2009**, *40*, 344.

[26] W. Zhang, B. Zhao, Z. He, X. Zhao, H. Wang, S. Yang, H. Wu, Y. Cao, *Energy Environ. Sci.* **2013**, *6*, 1956.

[27] Q. Chen, X. Li, X. Zang, Y. Cao, Y. He, P. Li, K. Wang, J. Wei, D. Wu, H. Zhu, *RSC Adv.* **2014**, *4*, 36253.

[28] M.-H. Pham, A. Khazaeli, G. Godbille-Cardona, F. Truica-Marasescu, B. Peppley, D. P. J. Barz, *J. Energy Storage* **2020**, *28*, 101210.

[29] S. Ling, W. Kang, S. Tao, C. Zhang, *Nano Mater. Sci.* **2019**, *1*, 142.

[30] B. Chen, Y. Jiang, X. Tang, Y. Pan, S. Hu, *ACS Appl. Mater. Interfaces* **2017**, *9*, 28433.

[31] P. Chen, H. Chen, J. Qiu, C. Zhou, *Nano Res.* **2010**, *3*, 594.

[32] Y. Xu, M. G. Schwab, A. J. Strudwick, I. Hennig, X. Feng, Z. Wu, K. Müllen, *Adv. Energy Mater.* **2013**, *3*, 1035.

[33] Y. Jiang, M. Cheng, R. Shahbazian-Yassar, Y. Pan, *Adv. Mater. Technol.* **2019**, *4*, 1900691.

[34] F. Tehrani, M. Beltrán-Gastélum, K. Sheth, A. Karajic, L. Yin, R. Kumar, F. Soto, J. Kim, J. Wang, S. Barton, M. Mueller, J. Wang, *Adv. Mater. Technol.* **2019**, *4*, 1900162.